JOURNAL OF SOLID STATE CHEMISTRY 111, 118–127 (1994)

Structural Refinement of the High Temperature Form of Bi_2MoO_6

D. J. Buttrey

Department of Chemical Engineering, University of Delaware, Newark, Delaware 19716

T. Vogt and U. Wildgruber

Physics Department, Bldg. 510B, Brookhaven National Laboratory, Upton, New York 11973

and

W. R. Robinson

Department of Chemistry, Purdue University, West Lafayette, Indiana 47907

Received January 14, 1994; accepted January 21, 1994

IN HONOR OF C. N. R. RAO ON HIS 60TH BIRTHDAY

The structure of the high temperature polymorph of Bi_2MoO_6 has been determined by Rietveld powder refinement of high-resolution neutron diffraction data from the H1A diffractometer at the Brookhaven HFBR (high flux beam reactor). The cation distribution forms a fluorite-related supercell with infinite channels of bismuth polyhedra surrounded by molybdenum tetrahedra, in agreement with previously proposed models. The structure is refined in the monoclinic space group $P2_1/c$ to $R_{wp} = 0.134$ and $R_I = 0.084$ ($R_{exp} = 0.024$) from 2559 reflections: $a = 17.2627(1)$ Å, $b = 22.4296(2)$ Å, $c = 5.58489(5)$ Å, $\beta = 90.4974(6)°$, $Z = 16$. Bond valence sums and site potentials have been calculated which reveal evidence for significant charge transfer in this structure. The relationship of this phase to other catalytically-active bismuth molybdates is discussed. © 1994 Academic Press, Inc.

INTRODUCTION

Bismuth molybdates are widely recognized as prototypical examples of catalysts for selective oxidation and ammoxidation of olefins (c.f. 1–4). A model case is the selective oxidation of propylene to produce acrolein with selectivities as high as 95%. This occurs by a two-step process (5) beginning with a rate-limiting hydrogen abstraction at a Bi site to generate a symmetrical allylic intermediate at an adjacent Mo site. In the second step, oxygen insertion from the Mo site produces the product acrolein. Although the Bi_2O_3–MoO_3 phase diagram has been examined by a number of groups (6–9), most of the reported phases have unknown crystal structures. In fact, the metal stoichiometry appears questionable for some, such as the high temperature phase reported as $Bi_6Mo_2O_{15}$ (10) by some and as $13Bi_2O_3$–$10MoO_3$ by others (11), yet with lattice parameters suggesting that these studies involve the same phase. This was also true for a phase initially reported as $3Bi_2O_3$–MoO_3 (4, 8, 12, 13) and later characterized by one of us as $Bi_{38}Mo_7O_{78}$ (14). In spite of uncertainties regarding composition and structure of many bismuth molybdates, it is apparent from electron and X-ray diffraction data that most of these materials may be viewed as having superstructures derived from a fluorite-like (pseudo-face centered cubic) subunit. The only reported exception to this is the case of the low temperature form of γ-Bi_2MoO_6, which is the natural mineral koechlinite and has a structure consisting of layers of corner-shared (distorted) MoO_6 octahedra separated by Bi_2O_2 bilayers.

Of the many known bismuth molybdate phases only three forms are recognized as active catalysts for selective oxidation and ammoxidation. These are the fluorite-related α-$Bi_2Mo_3O_{12}$ and β-$Bi_2Mo_2O_9$ phases with tetrahedrally coordinated molybdenum and the layered γ-Bi_2MoO_6 with distorted octahedrally coordinated molybdenum. With three catalytically active forms having similar Bi/Mo ratios (compared with others in the phase diagram), it seems somewhat surprising that there are no obvious structural features common to all. This is particularly surprising in view of the need for availability of lattice oxygen under catalytic conditions since the oxidation occurs sacrificially, requiring subsequent reoxidation of the catalyst. The fluorite-related structures should be particularly well suited to act as an oxygen reservoir and facilitate oxygen transport from the bulk to the surface. The layered γ-Bi_2MoO_6 may also be suitable in this regard since it is structurally a close relative of the K_2NiF_4 structure, with an additional layer of oxygen inserted into

0022-4596/94 $6.00

the "intercalation sites" within the rock salt component of that structure-type. This fully occupied layer of "intercalation sites" could provide an oxygen sink and, as with the fluorite family, may exhibit rapid oxygen transport at moderate temperatures. Nevertheless, the apparent lack of a common relationship between catalytic forms led us to examine the γ composition more closely, and motivates the present structural investigation.

For many years it has been known that at least two and most likely three polymorphic forms of Bi_2MoO_6 exist (15–18). Upon heating, the γ-phase (which is the mineral koechlinite) transforms by a reconstructive sequence beginning near 570°C, through an intermediate form, to a high temperature fluorite-related form usually designated as γ'-Bi_2MoO_6 or simply "gamma prime." According to a thermodynamic model proposed by Kodama and Watanabe (15), the (ambient pressure) transition from low to intermediate temperature forms occurs reversibly at 570°C, and from intermediate to high temperature forms slowly and irreversibly at 604°C. The intermediate polymorph has been reported as a layered structure closely related to the γ-phase and often designated as γ'' using Erman and Gal'perin's labels (18). The nearly irreversible nature of the transition from intermediate to high temperature forms conveniently makes it possible to quench the high temperature form to room temperature. The focus of our study is on the structure of this high temperature modification and its relationship to the α, β, and layered γ phases. From this point on we shall refer to the low, intermediate, and high temperature Bi_2MoO_6 phases as γ(L), γ(I), and γ(H), respectively, in accord the labeling used by Kodama and Watanabe (15) for the L and H forms.

The unit cell and qualitative structural features of the γ(H) phase are well established. The fluorite-like substructure ($a_{FCC} \approx 5.7 \pm 0.3$ Å) is clearly evident in both electron diffraction and X-ray powder diffraction data (9, 19). The unit cell edges are parallel to the pseudocubic subunit axes such that $a = 3a_F$, $b = 4b_F$ and $c = c_F$, where the subscript F represents the fluorite subunit. The structure also has a slight monoclinic distortion. Systematic absences evident in both the electron and X-ray diffraction data indicate that the space group is $P2_1/c$. Assuming full occupancy of cation sites, the 12 FCC subunits comprising the true unit cell account for 48 cations, such that $Z = 16$.

Two models for the γ(H) cation distribution have been proposed based on high resolution images (9, 17, 19). The model by Watanabe *et al.* (19) is derived from high resolution electron microscope (HREM) images in the [001] zone, which were not observed in an earlier HREM study by Buttrey *et al.* due to the highly elongated habit (9). The Watanabe result is consistent with an earlier sketch of the cation arrangement by van den Elzen and Rieck based on X-ray data and differs only in interchange of one Mo,Bi pair from that in Ref. (9). Both of these distributions are characterized by bismuth-rich tunnels parallel to c. In the Watanabe model the tunnel arrangement has the appearance of a "Latin cross," which is clearly evident in the contrast pattern of the [001] image. Raman data (20) show a strong antisymmetric stretching mode near 900 cm^{-1}, which is characteristic of tetrahedral MoO_4, for which we expect Mo–O distances averaging approximately 1.77 Å. By contrast, the antisymmetric stretch for octahedral MoO_6 is expected to appear closer to 800 cm^{-1}, as in the γ(L) Raman spectrum.

Starting with 4-circle X-ray diffraction data, we determined the cation distribution and tentative coordinates for some of the oxygen sites. Using these results, we generated a model placing the remaining oxygens in the ideal fluorite positions or in t_d coordination at 1.77 Å from the Mo sites. This model was then used as the starting point for refinement of the neutron powder data set. As we will show, the refined structure indeed does share very similar features with the α and β forms, provoking concern over which polymorphic form of Bi_2MoO_6 is really active under catalytic conditions.

EXPERIMENTAL

Materials Preparation

Although coprecipitation methods are commonly employed in producing high surface area specimens of the bismuth molybdates, Rastogi *et al.* (21) found that the reaction kinetics for Bi_2MoO_6(H) are sufficiently rapid for solid–solid reaction of the binary oxides to proceed efficiently to completion requiring no more than 5 hr at 580°C, in contrast with the slow kinetics of the transition from the γ(I) polymorph to γ(H) at lower temperatures. Egashira *et al.* (8) report that this transition rapidly accelerates between 600 and 620°C. For this reason, we chose to perform the synthesis by direct combination of the component binary oxides. A 15-g polycrystalline specimen of γ(H) was prepared by solid–solid reaction in air at 800°C from 99.9% Bi_2O_3 and 99.95% MoO_3 in an alumina crucible. The product was cooled rapidly to room temperature after 24 hr and subsequently pressed into two ~1 cm diameter pellets.

Small single crystals were grown from a molybdenum-rich melt using the temperature gradient self-flux method in an alumina boat. Excess MoO_3 is needed due to the incongruent melting of the Bi_2MoO_6 composition at 947°C (7). The starting composition was set just below the peritectic composition and melting was observed visually through the gold-mirrored quartz wall furnace. A small secondary heating coil was used to induce the desired

temperature gradient. Seven matched Type-K thermocouples were placed alongside the boat at 1 cm intervals to monitor the temperature profile. The system was rapidly cooled when the temperature had dropped to near the peritectic point for β-$Bi_2Mo_2O_9$ (682°C) (7). The resulting crystals were transparent yellow needles and many appeared to be good single crystals when observed under polarized light.

X-Ray Single Crystal Structure Determination

Data were collected with an Enraf–Nonius CAD4 X-ray diffractometer using Mo$K\alpha$ radiation from a graphite monochromator. Twenty-four diffraction maxima were carefully centered and used to determine cell dimensions for data collection. Reflections were collected in the ω-scan mode with no allowance for systematic absences. Subsequent examination of the data for absences provided support for the expected space group $P2_1/c$ (No. 14). Examination of several dozen reflections in a hemisphere of reciprocal space confirmed that the diffraction symmetry was appropriate for this space group.

Bismuth and molybdenum atoms were located from a Patterson map and refined by the full matrix least-squares technique using the Enraf–Nonius SDP package supplied with the diffractometer system. Although possible oxygen locations were observed on subsequent Fourier maps, it was not possible to locate and satisfactorily refine a complete set of oxygen atoms. However, the bismuth and molybdenum positions appear robust and were taken as the initial heavy atom positions in the neutron refinement. Data collection parameters are reported in Table 1. Lattice constants have been omitted since the values obtained from refinement of the neutron powder data are significantly more reliable.

TABLE 1
X-Ray Crystallographic Data for γ(H)-Bi_2MoO_6

Approximate crystal dimensions	0.1 × 0.1 × 0.1 mm^3
Space group	$P2_1/c$ (No. 14)
Z	16
θ range	4°–25°
Maximum scan time	60 s
Scan angle	1 + 0.14 tan θ
Temperature	21°C
Standards	three, every 2 hr
Total data	3866
Unique data, $F_0^2 > 3\sigma(F_0^2)$	2237
Residuals;	
R	0.242
R_{wt}	0.193
Wt	$1/\sigma^2(F_0)^a$
Goodness of fit	4.2

[a] $1/\sigma^2(F_0) = 4F_0^2/\sigma^2(F_0^2)$; $\sigma(F_0^2) = [\sigma(F_0^2) + (0.05)F_0^2]^{1/2}$.

High-Resolution Powder Neutron Diffraction

Data were obtained on the new high-resolution neutron powder diffractometer (HRNPD) at beamline H1A of the high flux beam reactor (HFBR) at Brookhaven National Laboratory (BNL) (22). This instrument features a monochromator which is a 30 cm tall vertical focusing array of 24 Ge(115) composites at a take-off angle of 120°, providing a beam cross-section of 4.5 × 2.5 cm^2 and a wavelength of 1.8857 Å. The monochromator is positioned 4.56 m from the H1A exit beam. The connecting flight path is filled with argon to reduce scattering and contains a 5′ or 11′ primary collimators in front of the monochromator. For our measurement, the 5′ primary collimator was used. The composites and general design of the monochromator have been described in detail elsewhere (23, 24). The sample is positioned 2.57 m from the monochromator as a container-free pressed pellet approximately 1 cm in diameter by 2 cm in height. The flight path from the monochromator to the specimen is through air.

The HRNPD is equipped with a detector bank positioned 99 cm from the specimen and consisting of 64 individual ^{3}He detectors which are separated by 2.5°. In front of each detector is a 5′ collimator. The entire detector bank was moved in 0.02° steps with integration times of roughly 5 min per step. Blocks of intensity and position data were then normalized with respect to both detector efficiency and positional errors.

The data consisted of 7250 points from 10 to 154.98° in steps of 0.02°. The data were refined using the modern Rietveld (25) refinement program PROFIL written by J. K. Cockcroft. A total of 146 parameters were refined, 137 of which were structural parameters. The total number of reflections used was 2559. To obtain accurate structural parameters, prior chemical knowledge of the Mo–O distances was initially introduced into the refinement by the use of chemical constraints. PROFIL allows for this type of refinement, where the minimized quantity then depends on the fit to the diffraction profile and the imposed model. This is a well established technique in crystallography (26) and has been used successfully in powder diffraction both to solve (27) and to refine structures (28). Sixteen individual bond distances were constrained at 1.77 ± 0.05 Å, corresponding to one for each distinguishable tetrahedral Mo–O bond. This rather relaxed chemical constraint, which is consistent with the observed Raman spectrum (20), was used to reduce the parameter space in such a complex structure.

RESULTS AND DISCUSSION

The results of the neutron powder data refinement are presented in Table 2 and the fit to the powder pattern in Fig. 1. The cation coordinates are in good agreement

TABLE 2
Neutron Powder Refinement Parameters for γ(H)–Bi_2MoO_6

Atom	x	y	z	B(iso)
Bi(1)	0.0950(3)	0.1934(2)	0.003(1)	0.247(3)
Bi(2)	0.2581(3)	0.0713(2)	0.018(1)	0.247(3)
Bi(3)	0.2566(3)	0.1877(3)	0.424(1)	0.247(3)
Bi(4)	0.4084(3)	0.0676(2)	0.504(1)	0.247(3)
Bi(5)	0.4089(3)	0.1891(2)	0.934(1)	0.247(3)
Bi(6)	0.5701(3)	0.1927(2)	0.520(1)	0.247(3)
Bi(7)	0.7423(3)	0.1956(2)	0.997(1)	0.247(3)
Bi(8)	0.9094(3)	0.0643(2)	0.018(1)	0.247(3)
Mo(1)	0.0831(5)	0.0580(3)	0.495(1)	1.16(1)
Mo(2)	0.5888(5)	0.0708(3)	0.011(1)	1.16(1)
Mo(3)	0.7704(4)	0.0611(4)	0.498(1)	1.16(1)
Mo(4)	0.9185(5)	0.1818(3)	0.511(1)	1.16(1)
O(1)	0.0265(5)	0.1009(4)	0.309(1)	0.519(1)
O(2)	0.0311(4)	0.0252(4)	0.733(1)	0.519(1)
O(3)	0.1516(5)	0.2463(4)	0.751(1)	0.519(1)
O(4)	0.3276(5)	0.1152(3)	0.754(1)	0.519(1)
O(5)	0.3309(5)	0.2501(4)	0.754(1)	0.519(1)
O(6)	0.6354(5)	0.0066(3)	0.125(1)	0.519(1)
O(7)	0.5081(5)	0.0959(4)	0.199(1)	0.519(1)
O(8)	0.5133(5)	0.2508(4)	0.769(1)	0.519(1)
O(9)	0.5431(5)	0.0442(4)	0.739(1)	0.519(1)
O(10)	0.6372(5)	0.1360(3)	0.917(1)	0.519(1)
O(11)	0.6764(5)	0.2482(4)	0.242(1)	0.519(1)
O(12)	0.7037(5)	0.0066(4)	0.624(1)	0.519(1)
O(13)	0.8226(5)	0.0227(3)	0.270(1)	0.519(1)
O(14)	0.8159(4)	0.0984(4)	0.765(1)	0.519(1)
O(15)	0.8432(5)	0.2285(4)	0.616(1)	0.519(1)
O(16)	0.8710(5)	0.1380(3)	0.286(1)	0.519(1)
O(17)	0.1363(5)	0.0104(4)	0.280(1)	0.519(1)
O(18)	0.1987(4)	0.1520(4)	0.102(1)	0.519(1)
O(19)	0.1526(5)	0.1026(4)	0.625(1)	0.519(1)
O(20)	0.3349(5)	0.1148(3)	0.258(1)	0.519(1)
O(21)	0.4610(5)	0.1518(4)	0.600(1)	0.519(1)
O(22)	0.7076(5)	0.1158(4)	0.370(1)	0.519(1)
O(23)	0.9901(5)	0.2273(4)	0.390(1)	0.519(1)
O(24)	0.9562(2)	0.1440(4)	0.775(1)	0.519(1)
R_{wp} = 13.4%		R_{exp} = 2.4%		R_I = 8.4%

Note. Space group: $P2_1/c$(#14) ($Z = 4$). Cell constants: a = 17.2627(1) Å, b = 22.4296(2) Å, c = 5.58489(5) Å, β = 90.4974(6)°. Cell volume: 2162.35(4) Å^3. Calculated density: 7.493 g/cm^3.

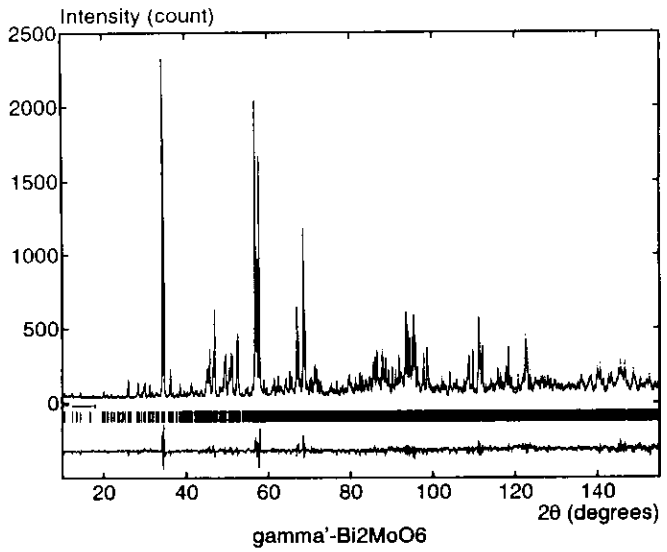

FIG. 1. Rietveld refinement plot of γ(H)-Bi_2MoO_6. Tick marks indicate the location of individual Bragg reflections. Lower curve is the difference curve between observed and calculated profiles.

with the fluorite-related cation distribution proposed by Watanabe *et al.* (19). The individual bond lengths and angles for the molybdenum coordination environments are presented in Table 3, and the structure is illustrated in Fig. 2. As expected, the molybdenum coordination is nearly regular tetrahedral for each site. The bismuth coordination environments are less regular with wide variations in O–Bi–O bond angles as listed in Table 4. In several cases there are rather short Bi–O bond lengths (~2.15 Å) associated with a given oxygen to two or three neighboring Bi sites. Valence bond sums and Madelung site potentials have been determined using the program EUTAX (29). The valence sums are obtained by first determining bond valences as

$$v_{ij} = \exp[(R_0 - d_{ij})/0.37],$$

where values for R_0 are the valence bond parameters for each bond pair and d_{ij} are the actual bond lengths. Values for R_0 used in this program are taken from those tabulated by Brown and Altermatt (30):

Bi–O	R_0 = 2.094 Å
Mo–O	R_0 = 1.907 Å
O–O	R_0 = 1.480 Å.

Valence bond sums are then obtained by simply summing over all neighbors for each of the sites:

$$V_i = \sum_j v_{ij}.$$

Several of the oxygen atoms have anomalously high valence bond sums and low site potentials (Table 5). In each instance these are associated with oxygens having short bonds to Bi. This is illustrated in Fig. 3, which is a bonding graph showing cation–anion connectivity out to separations of 4.0 Å. The heavy lines represent short bond lengths, using $v_{ij} > 0.65$ as the criterion for both Bi–O and Mo–O bonds (corresponding to bonds with $d_{ij} \leq 2.253$ Å for Bi–O and $d_{ij} \leq 2.066$ Å for Mo–O). Dashed lines indicate long bonds for which $v_{ij} \leq 0.16$ and the thin solid lines represent intermediate cases. As expected, this illustration shows the four near neighbors to each tetrahedral Mo site. Each of the Bi sites within the Latin cross,

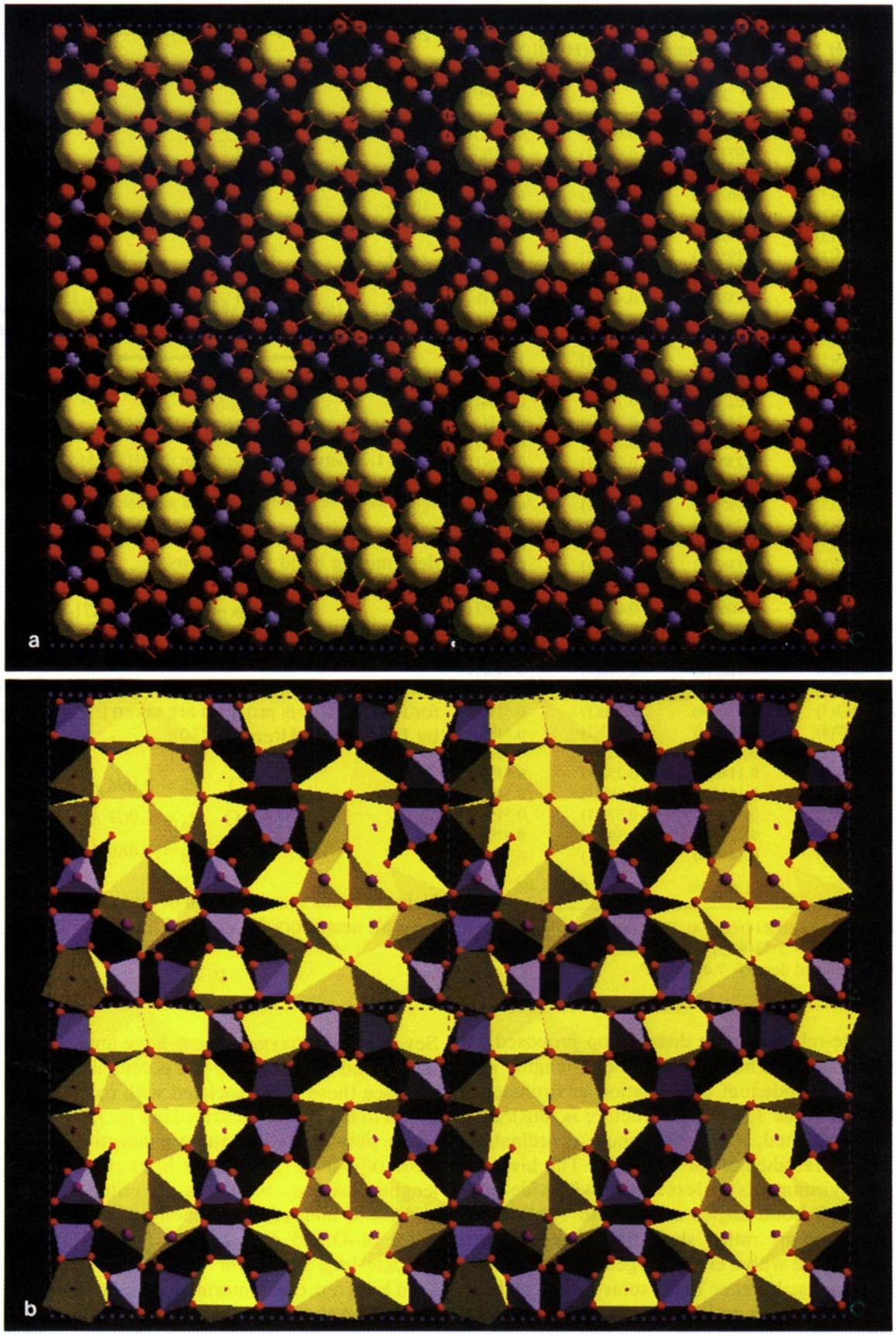
a
b

TABLE 3
Metal–Oxygen Interatomic Distances in Ångstroms

Bi(1)–O(18)	2.082(11)	Bi(3)–O(5)a	2.127(11)	Bi(5)–O(5)a	2.168(11)	Bi(7)–O(11)a	2.145(11)
Bi(1)–O(3)a	2.094(11)	Bi(3)–O(18)	2.202(10)	Bi(5)–O(21)	2.253(10)	Bi(7)–O(11)b	2.217(11)
Bi(1)–O(3)b	2.166(11)	Bi(3)–O(20)	2.325(10)	Bi(5)–O(4)	2.395(10)	Bi(7)–O(10)	2.311(10)
Bi(1)–O(23)a	2.611(11)	Bi(3)–O(3)a	2.523(11)	Bi(5)–O(8)a	2.450(11)	Bi(7)–O(15)a	2.516(11)
Bi(1)–O(24)	2.923(9)	Bi(3)–O(5)b	2.632(11)	Bi(5)–O(5)b	2.620(11)	Bi(7)–O(22)	2.821(11)
Bi(1)–O(23)b	2.927(11)	Bi(3)–O(4)	2.730(11)	Bi(5)–O(20)	2.769(10)	Bi(7)–O(14)	2.837(11)
Bi(1)–O(1)	2.940(11)	Bi(3)–O(19)	2.857(11)	Bi(5)–O(8)b	2.915(11)	Bi(7)–O(15)b	2.852(11)
Bi(1)–O(19)	3.108(11)	Bi(3)–O(3)b	2.901(11)	Bi(5)–O(7)	3.072(10)	Bi(7)–O(16)	3.023(10)
Bi(2)–O(20)	2.120(10)	Bi(4)–O(20)	2.143(11)	Bi(6)–O(8)a	2.132(11)	Bi(8)–O(13)	2.274(10)
Bi(2)–O(18)	2.147(10)	Bi(4)–O(21)	2.169(11)	Bi(6)–O(21)	2.141(10)	Bi(8)–O(14)	2.280(10)
Bi(2)–O(4)	2.150(10)	Bi(4)–O(4)	2.253(11)	Bi(6)–O(8)b	2.150(11)	Bi(8)–O(16)	2.341(10)
Bi(2)–O(6)	2.658(10)	Bi(4)–O(7)	2.518(10)	Bi(6)–O(11)a	2.564(11)	Bi(8)–O(24)	2.384(11)
Bi(2)–O(12)	2.730(10)	Bi(4)–O(12)	2.642(11)	Bi(6)–O(11)b	2.720(11)	Bi(8)–O(17)	2.480(11)
Bi(2)–O(13)	2.990(10)	Bi(4)–O(9)a	2.706(11)	Bi(6)–O(10)	2.796(11)	Bi(8)–O(2)a	2.645(11)
Bi(2)–O(17)	2.916(10)	Bi(4)–O(6)	2.771(11)	Bi(6)–O(7)	3.014(11)	Bi(8)–O(1)	2.707(11)
Bi(2)–O(19)	2.927(10)	Bi(4)–O(9)b	2.968(11)	Bi(6)–O(22)	3.055(10)	Bi(8)–O(2)b	2.784(11)
Mo(1)–O(19)	1.718(12)	Mo(2)–O(10)	1.751(12)	Mo(3)–O(22)	1.777(12)	Mo(4)–O(23)a	1.747(12)
Mo(1)–O(1)	1.719(12)	Mo(2)–O(6)	1.764(12)	Mo(3)–O(13)	1.781(12)	Mo(4)–O(15)a	1.771(12)
Mo(1)–O(2)a	1.765(12)	Mo(2)–O(9)a	1.819(12)	Mo(3)–O(12)	1.823(12)	Mo(4)–O(16)	1.787(12)
Mo(1)–O(17)	1.854(12)	Mo(2)–O(7)	1.835(12)	Mo(3)–O(14)	1.871(12)	Mo(4)–O(24)	1.814(12)
Mo(1)–O(13)	2.759(12)	Mo(2)–O(22)	3.020(12)	Mo(3)–O(17)	2.591(12)	Mo(4)–O(1)	2.839(12)
Mo(1)–O(2)b	2.988(12)	Mo(2)–O(12)	3.283(12)	Mo(3)–O(16)	2.720(12)	Mo(4)–O(14)	2.942(12)
Mo(1)–O(24)	3.320(11)	Mo(2)–O(21)	3.659(12)	Mo(3)–O(6)	3.347(12)	Mo(4)–O(23)b	3.176(12)
Mo(1)–O(18)	3.651(12)	Mo(2)–O(9)b	3.725(12)	Mo(3)–O(10)	3.692(12)	Mo(4)–O(15)b	3.251(12)

i.e., Bi(1)–(7), has two or three short bonds to oxygen, whereas the isolated Bi(8) site has a more nearly regular fluorite environment with one marginally distant and seven intermediate length neighbors. The oxygen sites involved in short bonds with Bi are represented in bold in this illustration to aid in comparison with Table 5. The valence bond sums exceed the formal valence and Madelung site potentials are anomalously low for these sites. A c-axis projection of half of the unit cell is presented in Fig. 4 with the Latin cross arrangement outlined. Note that the oxygens with high valence sums and low site potentials all lie within or adjacent to the cross. These "violations" of the valence sum rule reflect the distortions in bonding required in the fluorite-like cross environment, which must be fully oxygenated (i.e., without oxygen vacancies) in order to compensate for the formally hexavalent Mo sites.

Comparing with the Bi–O channels present in the α and β forms, both of which have complete oxygen sublattices but have cation vacancies, we might expect to find consistent bond valence behavior. We consider first the α-$Bi_2Mo_3O_{12}$ structure. The structure has been refined both by single crystal X-ray diffraction (31) and by neutron powder refinement (32). In Table 6, we list the valence sums and site potentials calculated from the neutron data refinement reported in Ref. (32). Similar results (not shown) were obtained from the refined coordinates from Ref. (31). Except for O(6), which has no short bonds to Bi but one intermediate at 2.33 Å, all high valence sum oxygens are associated with a single short bond to Bi: from Ref. (32), Bi(1)–O(10) is 2.220 Å, Bi(2)–O(2) is 2.165 Å, and Bi(2)–O(7) is 2.188 Å. Unlike γ(H)-Bi_2MoO_6, the site potentials are not low for these oxygens, apparently because of the much smaller cross-sections for the bismuth channels, which do not fully isolate any of the oxygens. When viewed in projection along the channel axes, each channel is only two Bi sites across. The β-$Bi_2Mo_2O_9$ structure has larger bismuth channels, having a "square" cross-section consisting of four Bi sites in projection along the channel axis (Fig. 5). Using the single crystal X-ray refinement data from Chen and Sleight (33) and correcting a misprint in the z-coordinate for Mo(1) as provided by A. Sleight (34), we have again calculated valence sums and site potentials (Table 7).

In particular, those oxygens with three relatively short bonds to Bi have the largest valence bond sums. Compar-

FIG. 2. Color representations of the γ(H)-Bi_2MoO_6 structure viewed in projection down the c-axis emphasizing (a) the "Latin-cross" cation distribution and (b) the arrangement of coordination polyhedra. The molybdenum sites are represented in blue and bismuth sites in yellow. Oxygen sites are represented as red or violet spheres smaller in size than the cations.

TABLE 4
Selected Oxygen–Metal–Oxygen Bond Angles

O(**3**)b–Bi(1)–O(**18**)	74.15(35)	O(1)–Mo(1)–O(17)	102.33(59)
O(**3**)a–Bi(1)–O(**3**)b	82.24(40)	O(17)–Mo(1)–O(19)	105.11(55)
O(**3**)a–Bi(1)–O(**18**)	91.49(36)	O(2)–Mo(1)–O(19)	106.40(60)
		O(1)–Mo(1)–O(19)	108.70(61)
O(**20**)–Bi(2)–O(**18**)	76.63(32)	O(1)–Mo(1)–O(2)	113.29(58)
O(**4**)–Bi(2)–O(**20**)	82.69(37)	O(2)–Mo(1)–O(17)	120.36(60)
O(**4**)–Bi(2)–O(**18**)	91.99(37)	ave	109.36
O(**18**)a–Bi(3)–O(<u>20</u>)	71.28(32)	O(6)–Mo(2)–O(9)	102.71(55)
O(**5**)a–Bi(3)–O(<u>20</u>)	85.88(36)	O(9)–Mo(2)–O(10)	102.84(57)
O(**5**)a–Bi(3)–O(**18**)a	98.36(39)	O(7)–Mo(2)–O(9)	104.29(55)
		O(7)–Mo(2)–O(10)	106.74(56)
O(**4**)–Bi(4)–O(**21**)	72.12(34)	O(6)–Mo(2)–O(7)	113.11(56)
O(**4**)–Bi(4)–O(**20**)	78.27(37)	O(6)–Mo(2)–O(10)	124.67(58)
O(**20**)–Bi(4)–O(**21**)	88.42(38)	ave	109.06
O(4)–Bi(5)–O(**5**)a	83.23(35)	O(12)–Mo(3)–O(22)	103.52(50)
O(**5**)a–Bi(5)–O(8)a	85.70(36)	O(12)–Mo(3)–O(14)	104.58(53)
O(**5**)a–Bi(5)–O(**21**)	95.86(38)	O(14)–Mo(3)–O(22)	105.15(60)
O(8)a–Bi(5)–O(**21**)	66.24(33)	O(12)–Mo(3)–O(13)	105.78(60)
O(4)–Bi(5)–O(**21**)	68.22(32)	O(13)–Mo(3)–O(22)	111.01(55)
		O(13)–Mo(3)–O(14)	124.75(51)
		ave	109.13
O(**8**)b–Bi(6)–O(**21**)	73.63(34)		
O(**8**)a–Bi(6)–O(**8**)b	81.64(40)	O(15)–Mo(4)–O(16)	102.87(59)
O(**8**)a–Bi(6)–O(**21**)	89.51(34)	O(15)–Mo(4)–O(24)	105.62(60)
		O(15)–Mo(4)–O(23)	107.68(56)
O(<u>10</u>)–Bi(7)–O(**11**)b	78.76(37)	O(23)–Mo(4)–O(24)	110.11(56)
O(**11**)a–Bi(7)–O(**11**)b	79.87(39)	O(16)–Mo(4)–O(23)	111.58(61)
O(<u>10</u>)–Bi(7)–O(**11**)a	91.25(38)	O(16)–Mo(4)–O(24)	118.07(57)
		ave	109.32

Note. Short ($d_{ij} \leq 2.255$) and intermediate ($2.255 < d_{ij} \leq 2.350$ Å) bonds between oxygen and bismuth are represented using bold and underscored numbers for the oxygens, respectively. Note that the ideal fluorite angles are 70.53°, 109.47°, and 180° for adjacent, opposite (t_d), and diagonally opposed neighbors.

ing the valence bond sums and site potentials calculated for the other fluorite-type bismuth molybdate structures which have been refined, i.e., α-$Bi_2Mo_3O_{12}$ and β-$Bi_2Mo_2O_9$, with our results we find similar anomalies. As evident from the results in Tables 5 and 6, anomalously large valence sums and low site potentials are apparent for several of the oxygens, suggesting that there is substantial hole character to these. In each case, the oxygens involved have very short bonds to one or more Bi neighbors. As the Bi/Mo ratio increases, the fluorite-like tunnel size increases and the number of oxygens without Mo neighbors and with short Bi–O bonds increases. Only in the γ' phase do we find short bonds from oxygen to three neighboring Bi sites and these sites have particularly low potentials. It seems that the hole character arises from charge transfer from the Bi channel region to the surrounding Mo tetrahedral environment. Oxygens which are not associated with the Bi channel and which are between channels in the *a* direction form a band roughly parallel to *b*, wiggling somewhat due to the asymmetric character of the cross and the screw condition; they have high site potentials suggesting that Mo(1) and Mo(4) may be slightly reduced.

The O–Bi–O angles involving the triplets of short Bi–O bonds for the channel bismuth sites are all adjacent (see Table 4) such that a sterically restricted cone is formed which points inward toward the Latin-cross channel axis. This steric restriction suggests that the Bi^{3+} one pairs are most likely pointed in a direction roughly opposite the cone axes and therefore outward from the channel axis. Another (related) indication of probable lone pair location

TABLE 5
Valence Bond Sums (V_i) and Madelung Site Potentials (U_i) for γ(H)-Bi_2MoO_6

Atom	V_i	U_i
Bi(1)	3.484	−31.08
Bi(2)	3.400	−33.78
Bi(3)	3.170	−41.82
Bi(4)	3.356	−39.01
Bi(5)	2.905	−44.25
Bi(6)	3.424	−39.73
Bi(7)	2.991	−28.30
Bi(8)	3.146	−20.05
Mo(1)	6.105	−50.53
Mo(2)	5.500	−60.46
Mo(3)	5.391	−51.58
Mo(4)	5.819	−50.35
†O(1)	2.041	37.61
†O(2)	1.892	38.64
*O(3)	2.266	13.84
*O(4)	2.149	9.83
*O(5)	2.222	5.41
O(6)	1.848	25.60
O(7)	1.680	19.11
*O(8)	2.268	7.12
O(9)	1.591	21.52
O(10)	2.190	26.38
*O(11)	2.065	16.04
O(12)	1.652	26.70
†O(13)	2.205	36.65
†O(14)	1.908	34.86
†O(15)	1.885	33.60
†O(16)	2.098	37.88
†O(17)	1.773	35.69
*O(18)	2.664	15.34
O(19)	1.959	28.74
*O(20)	2.518	10.67
*O(21)	2.375	7.89
O(22)	1.660	29.59
†O(23)	1.936	33.08
†O(24)	1.831	35.40

Note. Oxygens with unusually low Madelung site potentials (≤16 V) are indicated by (*) and those with high site potentials are indicated by (†).

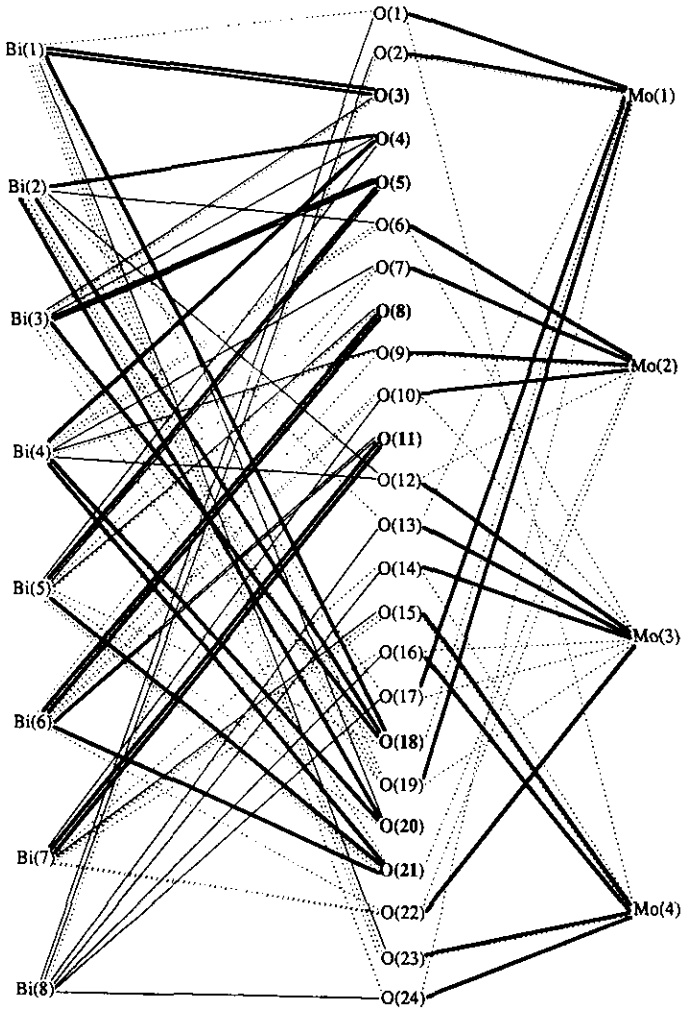

FIG. 3. Bonding diagram for γ(H)-Bi_2MoO_6. Heavy lines indicate short bond lengths, light lines indicate intermediate length bonds, and dashed lines represent more distant bonds within the fluorite-type coordination environment.

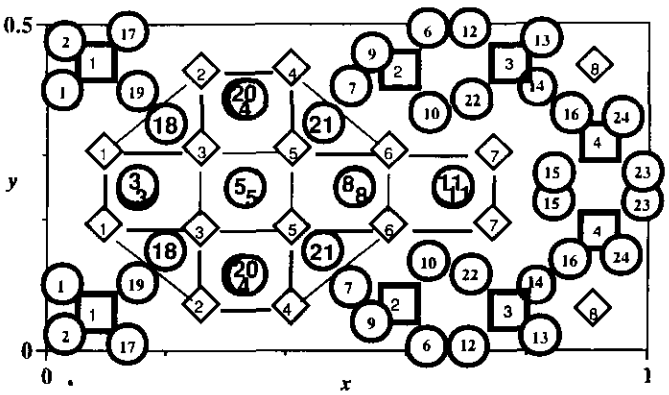

FIG. 4. Half of the unit cell of γ(H)-Bi_2MoO_6 viewed in projection down the c-axis (neglecting the small monoclinic distortion). Circles represent oxygen sites, squares are molybdenum sites, and diamonds are bismuth sites. Those oxygen sites indicated with two numbers represent two different sites which overlap in this projection. The Latin-cross channel is outlined and oxygen sites with low site potentials are labeled with enlarged numbers (i.e., 2–5, 8, 11, 18, 20, and 21).

may be obtained from calculation of the valence vector associated with the coordination environment about each Bi site. Presumably, the lone pairs should be positioned roughly opposite the direction of the valence vector. This analysis leads again to the conclusion that the lone pairs are directed away from the Latin-cross channel axis. The coordination environment about Bi(8) is more uniform 8-fold than that of the others, with no short bonds, so that no obvious steric indications of the lone pair orientation can be obtained; however, a valence vector of smaller magnitude than those of the other Bi sites suggests that the lone pair is probably oriented nearly parallel to c. A similar analysis of valence vectors for Bi sites in β-$Bi_2Mo_2O_9$ suggests that the lone pairs are again directed outward from the "square channel" axis for Bi sites 1, 2, and 4, whereas Bi(3), which is surrounded by MoO_4 tetrahedra and nearly uniformly coordinated by eight oxygens (similar to Bi(8) in γ(H)), has a smaller valence vector which suggests that the lone pairs alternate between $+z$ and $-z$ directions from site to site along b (see Fig. 5). Thus, the γ(H) and β structures have strikingly similar features, not only sharing common fluorite-type cation arrangements, but also having similarities in channel structure, site potentials, valence sums, lone pair orientation, etc. Exten-

TABLE 6
Valence Bond Sums (V_i) and Madelung Site Potentials (U_i) for α-$Bi_2Mo_3O_{12}$

Atom	x	y	z	V_i	U_i
Bi(1)	0.2552	0.3612	0.2607	3.163	−30.89
Bi(2)	0.9055	0.1314	0.0840	3.442	−31.63
Mo(1)	0.0254	0.1122	0.4150	5.718	−59.25
Mo(2)	0.4288	0.1496	0.1037	5.969	−60.13
Mo(3)	0.7325	0.3685	0.1943	5.805	−59.29
O(1)	0.5436	0.0503	0.2189	1.900	24.59
+O(2)	0.9362	0.0527	0.2556	2.234	26.11
O(3)	0.2158	0.1969	0.1543	1.943	22.15
O(4)	0.8525	0.2074	0.4126	1.931	27.01
O(5)	0.2308	0.2002	0.4441	1.667	25.57
O(6)	0.6068	0.2003	0.0588	2.195	29.48
+O(7)	0.9491	0.2874	0.1968	2.379	27.22
O(8)	0.5052	0.3166	0.1974	2.020	28.32
O(9)	0.2877	0.4405	0.4811	1.998	25.94
+O(10)	0.1294	0.4492	0.0783	2.117	27.50
O(11)	0.8313	0.4478	0.3372	1.603	23.21
O(12)	0.6827	0.4690	0.0873	2.110	25.33

Note. The structural data used here are from the neutron powder refinement results of Theobald *et al.* (32). Lattice constants are a = 7.7104 Å, b = 11.5313 Å, c = 11.9720 Å, and β = 115.28° (space group $P2_1/c$ and Z = 4). The (+) denotes oxygen sites with short bonds to bismuth, using the criterion $d_{ij} \leq 2.255$ Å.

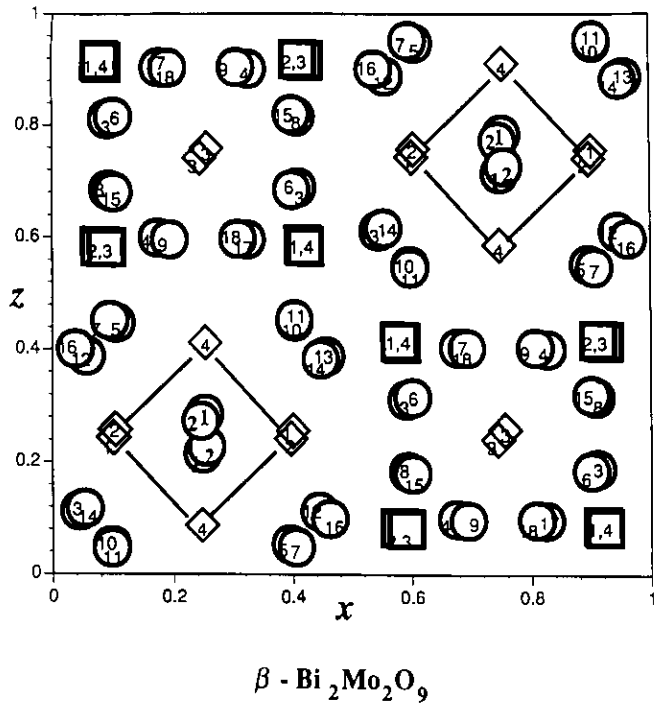

FIG. 5. Projection of the unit cell of β-$Bi_2Mo_2O_9$ viewed down the b axis. Circles represent oxygen sites, squares are molybdenum sites, and diamonds are bismuth sites. Those oxygen sites indicated with two numbers represent two different sites which overlap in this projection. The "square" channels are outlined and oxygen sites with low site potentials are labeled with enlarged numbers (i.e., 1 and 2).

sion of the comparison to the α-phase is less striking as a consequence of the smaller channel cross-section in that structure.

Although the γ(L) structure is layered and less obviously related to the others in the phase diagram, it is interesting to examine the bonding for comparison. Bond valence sums and site potentials were calculated from the structural refinement data of Teller *et al.* (35) and are presented in Table 8. Again, the oxygen sites which are coordinated only to bismuth, i.e., O(2) and O(3), have very low site potentials (~15 V) and high valence sums, whereas the others are closer to typical values. Comparison of the γ(L) structure with that of γ(H) suggests that the polymorphic transition probably involves a rearrangement of the Bi_2O_2 layer of the former to generate rows of Latin cross channels in the latter. This would suggest that the b-axis which is normal to the layers in γ(L) is common with the b-axis of γ(H) through the transformations via γ(I). Considering the similarities and differences between these γ forms, and their relationship with α and β, it is interesting to consider the importance of channels versus layers in the catalytic properties and in particular the role of low site potential oxygens in facilitating the hydrogen abstraction process. In view of these relationships it appears that the actual structure of the γ-

TABLE 7

Valence Bond Sums (V_i) and Madelung Site Potentials (U_i) for β-$Bi_2Mo_2O_9$ Calculated from Refined Coordinates of Chen and Sleight (33, 34)

Atom	x	y	z	V_i	U_i
Bi(1)	0.8998	0.1209	0.7564	2.942	−32.69
Bi(2)	0.6033	0.1229	0.7583	2.904	−32.97
Bi(3)	0.2558	0.1232	0.7585	3.064	−29.70
Bi(4)	0.2530	0.1228	0.4122	3.179	−32.09
Mo(1)	0.9173	0.1230	0.0877	6.027	−58.73
Mo(2)	0.9216	0.1250	0.4163	6.421	−59.23
Mo(3)	0.5893	0.1272	0.0814	6.187	−59.43
Mo(4)	0.5791	0.1321	0.4156	6.188	−58.32
*O(1)	0.252	0.2610	0.2850	2.396	15.18
*O(2)	0.255	0.493	0.2270	2.333	14.88
O(3)	0.409	0.257	0.689	1.965	28.36
O(4)	0.326	0.259	0.901	2.191	27.40
O(5)	0.105	0.437	0.447	2.069	25.32
O(6)	0.101	0.251	0.815	2.074	28.82
O(7)	0.405	0.444	0.048	2.052	27.77
O(8)	0.093	0.494	0.684	2.005	27.49
O(9)	0.194	0.260	0.596	2.030	29.18
O(10)	0.097	0.313	0.050	1.987	26.89
O(11)	0.403	0.308	0.454	2.075	27.73
O(12)	0.056	0.187	0.388	2.057	27.12
O(13)	0.044	0.046	0.112	1.912	25.61
O(14)	0.447	0.066	0.383	2.012	27.56
O(15)	0.399	0.495	0.820	2.014	28.89
O(16)	0.962	0.300	0.599	1.834	25.54
O(17)	0.177	0.489	0.904	1.969	28.88
O(18)	0.192	0.988	0.903	1.936	26.68

Note. The lattice constants are a = 11.972 Å, b = 10.813 Å, c = 11.899 Å, and β = 90.13° (space group $P2_1/n$ and Z = 4). The asterisk denotes oxygen sites with short bonds to bismuth using the same criteria as used in analyses of γ(H)-Bi_2MoO_6 and α-$Bi_2Mo_3O_{12}$.

TABLE 8

Bond Valence Sums (V_i) and Madelung Site Potentials (U_i) for γ(L)-Bi_2MoO_6 Calculated from Refined Coordinates of Teller *et al.* (35)

Atom	x	y	z	V_i	U_i
Bi(1)	0.5190	0.4231	0.9830	3.150	−33.39
Bi(2)	0.4830	0.0786	0.9890	2.992	−33.13
Mo	0.0010	0.2479	0.0000	5.949	−57.33
O(1)	0.0490	0.1428	0.0910	1.996	25.90
*O(2)	0.2590	0.9956	0.2710	2.187	14.81
*O(3)	0.2420	0.5048	0.2720	2.392	15.21
O(4)	0.6950	0.2297	0.2510	2.019	32.34
O(5)	0.2070	0.2624	0.3600	1.844	31.57
O(6)	0.5720	0.3602	0.5750	1.653	24.26

Note. The lattice constants are a = 5.4822 Å, b = 16.1986 Å, and c = 5.5091 Å (space group $P2_1/n$ and Z = 4). The asterisk denotes oxygen sites with short bonds to bismuth using the same criteria as used in analyses of γ'(H)-Bi_2MoO_6 and α-$Bi_2Mo_3O_{12}$.

phase surface present during catalysis should be re-examined.

ACKNOWLEDGMENTS

We gratefully acknowledge support for the work at Brookhaven National Laboratory under Contract DE-AC02-76CH00016, Division of Materials Sciences, U.S. Department of Energy.

REFERENCES

1. R. K. Grasselli and J. F. Burrington, *Adv. Catal.* **30,** 133 (1981).
2. R. K. Grasselli, *J. Chem. Ed.* **63,** 216 (1986).
3. D. J. Hucknall, "Selective Oxidation of Hydrocarbons." Academic Press, New York (1974).
4. Ph. A. Batist, A. H. W. M. der Kinderen, Y. Leeuwenburgh, F. A. M. G. Metz, and G. C. A. Schuit, *J. Catal.* **12,** 45 (1968).
5. L. C. Glaeser, J. F. Brazdil, M. A. Hazle, M. Mehicic, and R. K. Grasselli, *J. Chem. Soc. Faraday Trans. 1* **81,** 2903 (1985).
6. R. Kohlmuller and J. P. Badaud, *Bull. Soc. Chim. Fr.* **10,** 3434 (1969).
7. T. Chen and S. Smith, *J. Solid State Chem.* **13,** 288 (1975).
8. M. Egashira, K. Matsuo, S. Kagawa, and T. Seiyama, *J. Catal.* **58,** 409 (1979).
9. D. J. Buttrey, D. A. Jefferson, and J. M. Thomas, *Philos. Mag. A* **53,** 897 (1986).
10. S. Miyazawa, A. Kawana, and H. Koizumi, *Mater. Res. Bull.* **9,** 41 (1974).
11. T. Chen and S. Smith, *J. Solid State Chem.* **10,** 288 (1975).
12. L. N. Belyaev and N. P. Smolyaninov, *Russ. J. Inorg. Chem. (Engl. Trans.)* **7,** 579 (1962).
13. A. C. A. M. Bleijenberg, B. C. Lippens, and G. C. A. Schuit, *J. Catal.* **4,** 581 (1965).
14. D. J. Buttrey, D. A. Jefferson, and J. M. Thomas, *Mater. Res. Bull.* **21,** 739 (1985).
15. H. Kodama and A. Watanabe, *J. Solid State Chem.* **56,** 225 (1985).
16. G. Blasse, *J. Inorg. Nucl. Chem.* **28,** 1124 (1966).
17. A. F. van den Elzen, L. Boon, and R. Metslaar, "Solid State Chemistry." Elsevier, Amsterdam, 1982.
18. L. Y. Erman and E. L. Gal'perin, *Russ. J. Inorg. Chem. Engl. Trans.* **13,** 487 (1968).
19. A. Watanabe, S. Horiuchi, and H. Kodama, *J. Solid State Chem.* **67,** 333 (1987).
20. F. D. Hardcastle and I. E. Wachs, *J. Phys. Chem.* **95,** 10,763 (1991).
21. R. P. Rastogi, A. K. Singh, and C. S. Shukla, *J. Solid State Chem.* **42,** 136 (1982).
22. T. Vogt, L. Passell, and J. D. Axe, to be published.
23. J. D. Axe, S. Cheung, D. E. Cox, L. Passell, and T. Vogt, *J. Neutron Res.*, 1994.
24. T. Vogt, L. Passell, S. Cheung, and J. D. Axe, *Nucl. Instrum. Meth.* 1993.
25. H. M. Rietveld, *J. Appl. Crystallogr.* **2,** 65 (1969).
26. J. Waser, *Acta Crystallogr.* **16,** 1091 (1963).
27. J. K. Cockcroft, A. N. Fitch, *Z. Kristallogr.* **184,** 123 (1988).
28. M. Czjzek, H. Fuess, and T. Vogt, *J. Phys. Chem.* **95,** 5255 (1991).
29. M. O'Keeffe, "EUTAX, Version 1.3." EMLab Software, Phoenix, AZ, 1993.
30. I. D. Brown and D. Altermatt, *Acta Crystallogr. Sect. B* **41,** 244 (1985).
31. A. F. van den Elzen and G. D. Rieck, *Acta Crystallogr. Sect. B* **29,** 2436 (1973).
32. Theobald, Laarif, and A. W. Hewat, *Mater. Res. Bull.* **20,** 653 (1985).
33. H. Y. Chen and A. W. Sleight, *J. Solid State Chem.* **63,** 70 (1986).
34. A. W. Sleight, private communication.
35. R. G. Teller, J. F. Brazdil, R. K. Grasselli, and J. D. Jorgensen, *Acta Crystallogr. Sect. C* **40,** 2001 (1984).